

Effect of transient solar wind pulses on atmospheric heating at Jupiter

J. N. Yates^{a,b,*}, N. Achilleos^{a,b}, P. Guio^{a,b}

^a*Department of Physics and Astronomy, University College London, Gower Street, London, UK*

^b*Centre for Planetary Sciences at UCL / Birkbeck, University College London, Gower Street, London, UK*

Abstract

Previously, we have presented the first study to investigate the response of the Jovian thermosphere to transient variations in solar wind dynamic pressure, using a coupled, azimuthally symmetric global circulation model coupled with a simple magnetosphere model. This work (Yates et al., 2012b) described the response of thermospheric flows, momentum sources, and the magnetosphere-ionosphere coupling currents to transient compressions and expansions in the magnetosphere. The present study describes the response of thermospheric heating, cooling and the auroral emissions to the aforementioned transient events. We find that transient compressions and expansions, on time scales ≤ 3 hours, cause at least a factor of two increase in Joule heating per unit volume. Ion drag significantly changes the kinetic energy of the thermospheric neutrals depending on whether the magnetosphere is compressed or expanded. These processes lead to local temperature variations ≥ 25 K and a ~ 2000 TW increase in the total power dissipated in the thermosphere. In terms of auroral processes, transient compressions increase main oval UV emission by a factor of ~ 4.5 whilst transient expansions increase this main emission by a more modest 37%. Both types of transient event cause shifts in the position of the main oval, of up to 1° latitude.

Keywords:

Jupiter, magnetosphere, thermosphere, aurora, heating

*Corresponding author: Tel.: +44 (0)20 7679 4349; fax: +44 (0)20 7679 2328.
Email address: japheth.yates.09@ucl.ac.uk (J. N. Yates)

1. Introduction

The Jovian upper atmospheric temperature is up to 700 K higher than that predicted by solar heating alone (Strobel and Smith, 1973; Yelle and Miller, 2004). This ‘energy crisis’ at Jupiter and the other giant planets has puzzled scientists for over 40 years. Different theories have been put forward to explain Jovian upper atmospheric heating: gravity waves (Young et al., 1997), auroral particle precipitation (Waite et al., 1983; Grodent and Gérard, 2001), Joule heating (Waite et al., 1983; Eviatar and Barbosa, 1984) and ion drag (Miller et al., 2000; Smith et al., 2005; Millward et al., 2005). None of the aforementioned studies have been able to fully account for the observations.

Magnetosphere-ionosphere (M-I) coupling models by Achilleos et al. (1998); Smith and Aylward (2009); Tao et al. (2009); Yates et al. (2012a) have all discussed steady-state heating and cooling terms in the Jovian thermosphere. Cowley et al. (2007) discussed ‘transient’ heating and dynamics in terms of power dissipated in the thermosphere via Joule heating and ion drag, as well as power used to accelerate magnetospheric plasma. Cowley et al. (2007) considered displacements of the Jovian magnetopause by $\sim 40 R_J$ (Jovian radii; $1 R_J = 71492 \text{ km}$). They found that, for compressions, there was a net transfer of power from magnetosphere to planet of $\sim 325 \text{ TW}$, due to the expected super-corotation of magnetospheric plasma. For expansions, Cowley et al. (2007) found that the power dissipated in the thermosphere (and used to accelerate magnetospheric plasma) increased by a factor of ~ 2.5 resulting from a large increase in azimuthal flow shear between the expanded magnetosphere and the thermosphere.

Melin et al. (2006) analysed infrared data from an auroral heating event observed by Stallard et al. (2001, 2002) (from September 8-11, 1998) and found that particle precipitation could not account for the observed increase in ionospheric temperature (940–1065 K). The combined estimate of Joule heating and ion drag increased from 67 mW m^{-2} (on September 8) to 277 mW m^{-2} (on September 11) resulting from a doubling of the ionospheric electric field (inferred from spectroscopic observations); this increase in heating was able to account for the observed rise in temperature. Cooling terms (by Hydrocarbons and H_3^+ emission) also increased during the event but only by $\sim 20\%$ of the total inferred increase in heating. Thus a net increase in

ionospheric temperature resulted. More detailed analysis showed that these cooling mechanisms would be unlikely to return the thermosphere to its initial temperature before the onset of subsequent heating events. Melin et al. (2006) thus concluded that the temperature increases could plausibly lead to an increase in equatorward winds, which transport thermal energy to lower latitudes (Waite et al., 1983).

Cowley et al. (2007) modelled the auroral response of the Jovian system to transient compression and expansion events. ‘Transient’ in this context refers to events on timescales of $\lesssim 3$ hours, during which the angular velocity of magnetospheric plasma is mainly determined by conservation of angular momentum. Cowley et al. (2007) found that the precipitating electron energy flux ($\sim 10\%$ of which is used to produce ultraviolet (UV) aurora) increases by two orders of magnitude at the open-closed field line boundary and decreases by $\sim 50\%$ at the ‘main auroral oval’ during a transient magnetospheric compression. Essentially the opposite occurs for an expansion event, where main oval emission increases by a factor of 30 whilst emission at the open-closed boundary is reduced by $\sim 98\%$. Observations of transient aurorae have been carried out by Clarke et al. (2009) and Nichols et al. (2009). They showed that near the arrival of a solar wind shock at Jupiter’s magnetopause (averaging an order of magnitude increase in solar wind dynamic pressure) the total UV auroral power doubled. Nichols et al. (2009) also showed that the location of the main oval shifted polewards by $\sim 1^\circ$ following the arrival of this shock, and that the increase in UV power was distributed evenly between the main oval and polar (high-latitude) emission. For solar wind rarefactions, these studies observed little or no change in total UV auroral power.

Here, we use the Yates et al. (2012b) (henceforth Paper 1) model to simulate how the Jovian aurora and thermospheric heating responds to transient variations in magnetospheric size (via changes in solar wind dynamic pressure). We employ this same methodology, as adapted in Paper 1; time-dependent plasma angular momentum profiles are used to represent changes in magnetospheric size. The response of thermospheric heating and aurora is subsequently investigated. The present work, along with Paper 1, are the first studies to model the Jovian thermospheric response to varying solar wind dynamic pressure using a global circulation model (GCM).

In section 2 we summarise the scientific background appropriate for this

study, as well as model details. In sections 3 and 4 we present and discuss our findings for the transient compression and expansion scenarios respectively. We describe our conclusions in section 5.

2. Scientific Background

2.1. Time-dependence of the Jovian system

Cowley and Bunce (2003a,b) and Cowley et al. (2007) were amongst the first studies to investigate the time-dependence of M-I coupling in the Jovian system. In this section we summarise the three time scales of relevance for this study which allow us to make simplifying assumptions. For a more detailed discussion the reader is referred Cowley et al. (2007) and Paper 1.

i) M-I coupling time scale: For the Jovian system the transfer of angular momentum from thermosphere to magnetosphere is estimated to occur on time scales of $\sim 5\text{--}20$ hours by Cowley and Bunce (2003a).

ii) Compression (and expansion) of the magnetosphere: Cowley and Bunce (2003a) and Cowley et al. (2007) estimated that magnetospheric size could change by as much as $\sim 40 R_J$ in $\sim 2\text{--}3$ hours. Since this figure is small compared to the M-I coupling time scale plasma angular momentum could be assumed constant during the modelled event.

iii) Thermospheric response time: There are currently two thermospheric response models proposed for transient changes in magnetospheric size: (i) Millward et al. (2005) found, using a GCM (Achilleos et al., 1998), that the thermosphere responds promptly (few tens of minutes), and (ii) thermosphere responds over a few days and is thus, considered to be unresponsive (Gong, 2005). We, however, make no assumptions about a thermospheric response time. We allow the GCM to respond independently to imposed variations in angular velocity of magnetospheric plasma.

2.2. Magnetosphere model

To investigate transient changes in magnetospheric size, we make use of two established magnetospheric models. These are:

i) The quiescent magnetosphere model: This component is axisymmetric and consists of an equatorial magnetic field profile (Nichols and Cowley, 2004) and a magnetospheric plasma angular velocity profile, which is a steady-state

solution of the Hill-Pontius equation (Hill, 1979; Pontius, 1997). This quiescent model has been presented in Nichols and Cowley (2004); Smith and Aylward (2009); Yates et al. (2012a) and Paper 1. As such, we will not discuss it herein and we refer the reader to the cited studies for further details.

ii) The transient magnetosphere model: This component is produced by perturbing the ‘quiescent’ equatorial magnetic field so as to predict its behaviour during a transient compression or expansion. As described in Cowley et al. (2007) we use the principle of magnetic flux conservation. We take the initial, quiescent field model and add a uniform southward (northward for expansion) perturbation field ΔB_z at each time step throughout the transient event. ΔB_z is calculated, as a function of magnetodisc radius $R_{MM}(t)$ (at each time step t) using the flux conservation condition as employed by Cowley et al. (2007)

$$-\pi R_{MM}(t)^2 \Delta B_z = 2\pi (F_e(R_{MM}(t)) - F_e(R_{MM}(t=0))). \quad (1)$$

Solving for ΔB_z gives

$$\Delta B_z = \frac{-2\Delta F}{R_{MM}(t)^2}, \quad (2)$$

where F_e is the initial equatorial flux function at time zero ($t=0$), $\Delta F = F_e(R_{MM}(t)) - F_e(R_{MM}(t=0))$ and $\Delta B_z < 0$ for a southward field perturbation. $t=0$ denotes the initial, steady state of the system.

Transient plasma angular velocity profiles $\Omega_M(R_{MM}(t))$ are obtained assuming that plasma angular momentum is conserved. This is further discussed in section 2.6.

2.3. Magnetosphere-ionosphere coupling

The coupling of the magnetosphere and ionosphere models, has been discussed in detail in previous studies by Smith and Aylward (2009); Yates et al. (2012a) and Paper 1. Thus, here, we only briefly present equations relevant to the current study. For further details on the modelling of M-I coupling the reader is referred to the cited studies.

Electric and magnetic fields, along with ion-neutral collisions, create ionospheric Pedersen currents flowing perpendicular to the direction of the planetary magnetic field at high latitudes (corresponding to the main auroral emission). These Pedersen currents are connected to the magnetosphere via field-aligned currents. Radial currents in the magnetosphere then close the ‘circuit’ connecting the magnetosphere to the ionosphere. $j_{\parallel i}(\theta_i)$ denotes field-aligned current (FAC) density just above the ionosphere at co-latitude θ_i . This quantity, when positive (upward from planet) corresponds to auroral electron precipitation. Since FAC closes the divergence in horizontal Pedersen current, we may write:

$$j_{\parallel i}(\theta_i) = -\frac{1}{2\pi R_i^2 \sin \theta_i} \frac{dI_P}{d\theta_i}. \quad (3)$$

The sign of $j_{\parallel i}(\theta_i)$ indicates FAC direction (positive upward from planet), R_i is the ionospheric radius and I_P is the height-integrated Pedersen current (Cowley et al., 2007; Smith and Aylward, 2009).

The final aspect of M-I coupling we examine in this study is the energy transfer from planetary rotation to the thermosphere and magnetosphere. The energy transferred to the magnetosphere is used to accelerate magnetospheric plasma towards corotation whilst the energy dissipated within the thermosphere is used for heating and increasing kinetic energy. The total power per unit area of the ionosphere transferred from planetary rotation P is the sum of atmospheric power P_A and magnetospheric power P_M dissipated per unit area (Hill, 2001). As shown by Smith et al. (2005) atmospheric power consists of two components: (i) Joule heating P_J and (ii) ion drag power P_D , some of may be viscously dissipated as heat. These power relations are:

$$P = \Omega_J \tau, \quad (4)$$

$$P_M = \Omega_M \tau, \quad (5)$$

$$P_A = (\Omega_J - \Omega_M) \tau, \quad (6)$$

$$P_J = (\Omega_T - \Omega_M) \tau, \quad (7)$$

$$P_D = (\Omega_J - \Omega_T) \tau, \quad (8)$$

where

$$\tau = \rho_i i_P B_i \quad (9)$$

represents the torque exerted by the $\mathbf{J} \times \mathbf{B}$ force per unit area of the ionosphere. Note that Ω_T is a weighted average, computed over altitude, of thermospheric angular velocity (see Yates et al. (2012a) and Smith and Aylward (2009) for more detail).

2.4. Auroral energies

Once FAC densities have been calculated, we can use the methods of Knight (1973) and Lundin and Sandahl (1978), as presented in Cowley et al. (2007), to calculate the enhanced precipitating electron energy flux E_f :

$$E_f = \frac{E_{f0}}{2} \left(\left(\frac{j_{||i}}{j_{||i0}} \right)^2 + 1 \right), \quad (10)$$

where E_{f0} is the unaccelerated electron energy flux, $j_{||i0}$ is the unaccelerated FAC density (or the maximum current that can be carried by the electrons in the absence of field-aligned potential drops) and $j_{||i}$ is the upward (positive) FAC density calculated using Eq. (3). To enable a comparison with similar, earlier studies, we use the same electron population values described in Cowley et al. (2007), which are based on observations by Scudder et al. (1981) and Phillips et al. (1993a,b). These parameters are presented in Table 1.

2.5. Thermospheric energy equations

In this study we represent the thermosphere with a GCM. The GCM solves the non-linear Navier-Stokes equations of energy, momentum and continuity, by explicit time integration (Müller-Wodarg et al., 2006). The GCM was originally created for Saturn (Müller-Wodarg et al., 2006; Smith and Aylward, 2008) and later modified to represent Jupiter (Smith and Aylward, 2009). The model assumes azimuthal symmetry, and is thus two-dimensional (pressure/altitude and latitude).

This study is focused on the response of atmospheric heating sources during transient events. Thus, we include only the atmospheric heating equations in this section (Smith (2006); see also Achilleos et al. (1998); Tao et al.

(2009)). For the Navier-Stokes equations on the thermospheric dynamics the reader is referred to Paper 1. The energy equation used in the GCM is:

$$\frac{\partial \psi}{\partial t} = q - \mathbf{u} \cdot \nabla_p \psi - w \frac{\partial \psi}{\partial p}, \quad (11)$$

with

$$\psi = T + U, \quad (12)$$

$$q = q_P + q_D + q_J + q_\eta + q_\kappa + q_\nu, \quad (13)$$

where ψ is the sum of specific kinetic (T) and internal (U) energies of the system. \mathbf{u} is the horizontal velocity and q is the sum of sources and sinks of heat. The second and third terms on the RHS represent advective energy terms. The individual components of q consist of the work done from: pressure gradients (q_P), ion drag (q_D), Joule heating (q_J), viscosity (q_η), thermal conduction (q_κ) and solar radiation (q_ν). w ($w = dp/dt$) is the convective time derivative of the atmospheric pressure p . The individual energy sources and sinks are expressed below:

$$q_P = -\mathbf{u} \cdot g \nabla_p z + \frac{w}{\rho_m}, \quad (14)$$

$$q_D = -\mathbf{u} \cdot \frac{1}{\rho_m} \mathbf{j} \times \mathbf{B}, \quad (15)$$

$$q_J = \frac{1}{\rho_m} \mathbf{j} \cdot \mathbf{E}^*, \quad (16)$$

$$q_\eta = g^2 \frac{\partial}{\partial p} \left(\eta \rho_m \mathbf{u} \cdot \frac{\partial \mathbf{u}}{\partial p} \right), \quad (17)$$

$$q_\kappa = \frac{\kappa}{\rho_m} \nabla_p^2 T + g^2 \frac{\partial}{\partial p} \left(\kappa \rho_m \frac{\partial T}{\partial p} \right), \quad (18)$$

where g is the acceleration due to gravity, z is altitude (above 300 km), ρ_m is the thermospheric density, \mathbf{j} , \mathbf{B} and \mathbf{E}^* are respectively the current, magnetic field strength and rest-frame electric field. Finally, η is the viscosity, κ is the thermal conductivity and T the temperature. The absorption of solar radiation is a small energy source in the current model (Smith, 2006). For details regarding the absorption of solar radiation the reader is referred to Moore et al. (2004) and Müller-Wodarg et al. (2006).

2.6. Obtaining the transient plasma angular velocity

As the calculation of plasma angular velocity in the transient regime has been discussed thoroughly in Paper 1, we shall only briefly summarise the main points in this section. The reader is referred to Paper 1 and/or Cowley et al. (2007) (on which our model is based) for a more detailed description of the transient magnetospheric angular velocity model.

We may assume conservation of the plasma’s angular momentum if we consider a solar wind shock or rarefaction which will cause the magnetosphere to compress or expand several tens of R_J on time scales of $\sim 2\text{--}3$ hours (Cowley et al. (2007) and Paper 1). This gives a plasma angular velocity profile $\Omega_M(\theta_i, t)$, at any time t (throughout the ‘pulse’ in solar wind pressure) of

$$\Omega_M(\theta_i, t) = \Omega_M(\theta_i, t=0) \left(\frac{\rho_e(\theta_i, t=0)}{\rho_e(\theta_i, t)} \right)^2, \quad (19)$$

where the notation $t=0$ and t denotes the initial (steady-state) and transient (at each time-step throughout the event) states respectively. $\rho_e(\theta_i, t)$ is the time-dependent equatorial radial distance which magnetically maps to a co-latitude θ_i . Note that the size of the magnetodisc $R_{MM}(t)$ in this study is determined using a Gaussian function (see section 2.6 in Paper 1) and that the full duration of the solar wind pulse is three hours. In sections 3 and 4 we present results pertaining to the initial steady-state, half-way through the pulse (point of maximum compression or expansion) and at the end of the pulse (where $R_{MM}(t)$ returns to the initial value $R_{MM}(t=0)$).

The magnetosphere in our model is divided into four regions (Yates et al. (2012a) and Paper 1). Region I represents the open field lines mapping to the polar cap; region II represents the outer magnetosphere; region III represents the middle magnetosphere (magnetodisc); and region IV is the inner magnetosphere, which we assume is fully corotating in steady state. Region III is shaded light grey as this is our main region of interest due to its dominant role in M-I coupling.

Plasma angular velocities (thin lines) and corresponding thermospheric angular velocities (thick lines) as functions of ionospheric latitude are shown in Fig. 1. This Figure and the system state labels are identical to Figure 2

from Paper 1; thus, we will only summarise the transient plasma angular velocity discussion.

Angular velocity profiles for our transient compression event are shown in Fig. 1a. The solid lines indicate our initial steady state, henceforth called ‘case CS’ (pre-Compression Steady-state). Dashed lines represent results midway through the event ($R_{MM}(t)$ is at a minimum) and are referred to as case CH (Compression Half-pulse). The dot-dashed lines indicate the system at the end of the transient pulse, case CF (Compression Full-pulse). Considering case CH, Ω_M super-corotates over most of regions IV and III. This has a number of consequences such as the corresponding increase in Ω_T , ionospheric current reversal in these regions and the reversal of momentum transfer between the thermosphere and magnetosphere (Cowley et al., 2007). The magnetospheric response from case CS to CH is rather large (factor of two increase in peak Ω_M) compared to the $\sim 3\%$ average increase in Ω_T ; this is due to the neutral thermosphere having a larger mass than the magnetospheric plasma region to which it maps, and thus a larger inertia. For case CF, $\Omega_M(CF) = \Omega_M(CS)$ but $\Omega_T(CF) \neq \Omega_T(CS)$; this demonstrates that there is a time lag in the response of the thermosphere compared to the magnetosphere during transient changes in solar wind dynamic pressure. After the pulse has subsided, the thermosphere remains perturbed relative to its steady state.

Fig. 1b shows angular velocity profiles corresponding to the transient expansion scenario. System state labels and line styles are as in Fig. 1a but the ‘C’ (Compression) is exchanged for an ‘E’ (Expansion) giving cases ES, EH and EF. In case EH, magnetospheric sub-corotation decreased drastically which consequently decreased Ω_T , albeit to a much lesser degree. As in the compression scenario, $\Omega_M(EF) = \Omega_M(ES)$ and $\Omega_T(EF) \neq \Omega_T(ES)$. We do, however, note that a small amount of current reversal is expected near the region III/II boundary due to $\Omega_M(EF) > \Omega_T(EF)$; this acts to effectively ‘pull’ the thermosphere back towards corotation after a period of substantial sub-corotation.

3. Magnetospheric Compressions

In this section we present auroral and thermospheric heating results for a transient magnetospheric compression event. We present results from

three phases throughout the transient event: i) Steady state (case CS with $R_{MM}=85 R_J$), ii) ‘half-pulse’ (case CH with $R_{MM}=45 R_J$) and, iii) ‘full-pulse’ (case CF with $R_{MM}=85 R_J$).

3.1. Auroral response

We begin by discussing how a transient magnetospheric compression affects the aurorae. Here we only discuss the effects on FAC densities and the energy flux carried by precipitating electrons. For the detailed response of global M-I coupling currents the reader is referred to Paper 1.

We begin our discussion by briefly summarising the response of FAC densities (see Paper 1 for detailed derivation). Fig. 2a shows FAC density as a function of latitude for cases CS (solid line), CH (dashed line) and CF (dot-dashed line, nearly coincident with CS). Magnetospheric regions (region III shaded) are separated by black dotted lines and the latitudinal size of a Hubble Space Telescope (HST) ACS-SBC pixel (0.03×0.03 arc sec) is represented by the dark grey rectangle (assuming that the magnetic axis of the Jovian dipole is perpendicular to the observer’s line of sight). We notice that between cases CS and CF there are only minor differences in FAC profiles. These differences result from the lag in response of the thermosphere to the transient pulse. For case CF, $\Omega_M(CF)=\Omega_M(CS)$ but $\Omega_T(CF) \neq \Omega_T(CS)$, meaning the thermosphere has not settled back to its steady state profile (due to its large inertia; see section 2.6 and Paper 1). Comparing case CS with CH, CH has: i) substantial current reversal in region III, ii) maximum FAC about twice that of case CS, iii) increased FAC at the region II/I boundary (although this result is sensitive to our assumed choice of uniform angular velocity in region II). The current reversal over $\sim 4^\circ$ of region III is a direct result of the super-corotation of Ω_M (see Fig. 1a) whilst the increases in upward FAC result from increases in the Pedersen current (see Paper 1) caused by an increase in flow shear ($\Omega_T - \Omega_M$).

Corresponding precipitating electron energy fluxes are shown in Fig. 2b. These fluxes are plotted as a function of latitude. The line style code and labels are the same as in Fig. 2a and the grey solid line indicates the limit of present detectability with HST instrumentation (~ 1 kR; Cowley et al. (2007)). These fluxes are obtained using Eq. (10), which uses only the upward (positive) FAC densities presented in Fig. 2a. We initially compare

electron energy fluxes for cases CS and CF. These profiles are identical poleward of $\sim 74^\circ$; equatorward of this location, case CF shows little deviation from CS, despite the thermospheric lag discussed in section 2.6. In region III, we find that the peak energy flux for case CF is $\sim 35\%$ larger than that in case CS and the location of these peaks coincides with the location of the main auroral oval ($\sim 74^\circ$). The slight increase in peak energy flux is due to a relative increase in flow shear as seen in Fig. 1a. Case CF would therefore produce main oval emission of approximately ~ 200 kR brighter than that of CS (assuming that 1 mW m^{-2} of precipitation creates ~ 10 kR of UV output (Cowley et al., 2007)). The main oval would also be $\sim 1.5^\circ$ broader for CF than for case CS.

The E_f profile for case CH is different from those of both cases CS and CF. There are three main changes in CH compared to CS: i) peak energy flux in region III is $\sim 280 \text{ mW m}^{-2}$, almost a factor of five larger, ii) location of peak energy flux has shifted polewards by $\sim 0.2^\circ$ and, iii) presence of a second peak with an energy flux of 1.7 mW m^{-2} at the region II/I boundary. The large increase in energy flux is caused by a substantial increase in flow shear between the thermosphere and magnetosphere, resulting from the super-corotation of the middle magnetosphere (see Fig. 1). The presence of a second peak at the region II/I boundary is also due to flow shear increase across the boundary, as the magnetosphere in region II corotates at a larger fraction of Ω_J compared to case CS. The result for this higher-latitude boundary should be regarded as preliminary, since it is sensitive to the values of Ω_M we assume in the outer magnetospheric region and polar cap. Flow velocities in these regions are poorly constrained by observations (Stallard et al., 2003).

Comparing the energy flux profile of case CH with the equivalent case in Cowley et al. (2007) (with a responsive thermosphere; they do not calculate energy fluxes for a non-responsive thermosphere), we see that in the closed field regions (III and II), peak energy fluxes are two orders of magnitude larger in case CH. This demonstrates the differences between using a GCM to represent the thermosphere or using a simple ‘slippage’ relation between thermospheric and magnetospheric angular velocities. At the open-closed field line boundary (II/I boundary) our peak flux is an order of magnitude smaller than that in Cowley et al. (2007); this difference arises from the different models used to represent the outer magnetosphere. The outer magnetosphere (region II) and open field line region (region I) in this study is

modelled using Cowley et al. (2005).

The increase in E_f for case CH would lead to corresponding increases in auroral emission. As such, we would expect ‘main oval’ emission for case CH to shift polewards by $\sim 0.2^\circ$ and be $\sim 4.7 \times$ larger than emission in case CS i.e. ~ 2800 kR compared to ~ 600 kR. Clarke et al. (2009) and Nichols et al. (2009) observed that the brightness of UV auroral emission increased by a factor of approximately two, in response to transient (almost instantaneous) increases in solar wind dynamic pressure (~ 0.01 – 0.3 nPa or equivalently ~ 109 – $72 R_J$). Nichols et al. (2009) also observed poleward shifts in main oval emission on the order of $\sim 1^\circ$ corresponding to the arrival of solar wind shocks. Total emitted UV power can be used to describe auroral activity, assuming that this quantity is $\sim 10\%$ of the integrated electron energy flux per hemisphere (Cowley et al., 2007). Case CH has a total UV power of ~ 1.58 TW (compared to ~ 420 GW for case CS), which is a factor of two to three times larger than UV powers observed by both Clarke et al. (2009) and Nichols et al. (2009). The profile of case CH also indicates the possibility of observable polar emission at region II/I (open-closed) boundary. This conclusion is, however, sensitive to our model assumptions.

3.2. Thermospheric heating

In this section, we present and discuss the response of thermospheric heating terms to our transient magnetospheric compression event. We present azimuthal and meridional flows and temperature differences (from steady state) in Fig. 3. The results in Fig. 3 have been discussed at length in Paper 1 and we therefore only describe the major flow patterns associated with zonal (Figs. 3a-c) and meridional flow (Figs. 3d-f). Thermospheric temperatures are presented in Figs. 3g-i and we use thermospheric heating terms and powers per unit area (Fig. 4) to aid in their discussion. For completion we also present integrated powers per hemisphere in Fig. 5. Cases CS-CF are represented in columns 1–3 of Figs. 3-4 respectively.

Figs. 3a-c show thermospheric azimuthal velocity, in the corotating reference frame, as a function of altitude and latitude for cases CS-CF. Positive velocities indicate super-corotation whilst negative velocities indicate sub-corotation. The white contour indicates the locus of rigid corotation, black contour indicates regions of strong super-corotation ($> 25 \text{ m s}^{-1}$), the

white dashed contour shows regions that are strongly ($> -2500 \text{ m s}^{-1}$) sub-corotating and the black arrows indicate the direction of meridional flow. Magnetospheric regions are labelled and separated by black dotted lines. The zonal flow patterns include: i) a low-altitude ($\sim 400 - 500 \text{ km}$) super-corotating jet, centred at $\sim 72^\circ$; and ii) a large sub-corotating jet, spanning region III - I (blue region in Figs. 3a-c). These general features are persistent throughout the transient compression event. Differences do arise in the speed of flows: where we see an increase in the degree of corotation (and super-corotation) in case CH (indicated by the area covered by the white-dashed contour having decreased and that covered by the black contour having increased). This is followed by a subsequent decrease super-corotation in case CF. We do however note that in regions II, there is a slight increase in corotation in case CF. Figs. 3d-f show thermospheric meridional velocity as a function of altitude and latitude for cases CS-CF. The arrows indicate the direction of the steady-state meridional flow pattern (Fig. 3d), where we have low altitude ($< 600 \text{ km}$) poleward flows and high altitude ($> 600 \text{ km}$) equatorward flows, as predicted by Smith et al. (2007); Smith and Aylward (2009) and Yates et al. (2012a). We also note the presence of localised accelerated regions (red/brown hues) which result from the advection of momentum (Yates et al., 2012a). The response of the meridional flows can be seen in Figs. 3d-f where flow patterns evolve with time to become quite complex. The number of local regions with strongly accelerated flows increases significantly with time. The reader is referred to Paper 1 for more detailed discussions on these flows and their causes.

Fig. 3g shows thermospheric temperature as a function of altitude and latitude for case CS. Figs. 3h-i show the difference in thermospheric temperature between cases CH and CS, and cases CF and CS. We will use Figs. 4a-f, showing contour plots for various thermospheric heating (Figs. 4a-c) and cooling (Figs. 4d-f) terms (see plot legends for details) to interpret the temperature response.

In Fig. 3g we see a clear temperature difference between upper ($> 75^\circ$) and lower ($< 75^\circ$) latitudes; lower latitudes are cooled whilst upper latitudes are significantly heated (Smith et al., 2007; Smith and Aylward, 2009). We see a ‘hotspot’ (in region I) with a peak temperature of $\sim 705 \text{ K}$. This arises from the poleward transport of Joule heating (from regions III and II) by the accelerated meridional flows shown in Fig. 3d (Smith and Aylward, 2009;

Yates et al., 2012a).

Fig. 3h shows the temperature difference between cases CH and CS. There are three prominent features in Fig. 3h:

i) Temperature increase up to ~ 26 K across the region III/II boundary ($z \geq 400$ km) resulting from a large ($\times 2$) increase in Joule heating and the addition of other heat sources, such as adiabatic heating (see Fig. 4b). The large increase in Joule heating is caused by the increase in FAC and the rest-frame electric field (see Fig. 2a and Paper 1 respectively).

ii) Temperature decrease down to ~ -22 K, at low altitudes of region II. Fig. 4b shows that at low altitudes (≤ 500 km) of region II there is, on average, a 20 % decrease in energy deposited by Joule heating and ion drag. This, coupled with the presence of energy lost by ion drag (Fig. 4e) in this region causes the significant decrease in temperature shown above. All the factors discussed above result from the reversal and decrease (in magnitude) of the flow shear between the magnetosphere and thermosphere in case CH.

iii) A maximum of ~ 17 K increase at low altitudes in region I. The meridional velocity of case CH increases slightly (~ 2 %) in this region and, as such, can transport heat from Joule heating and ion drag polewards more efficiently than in case CS.

Fig. 3i shows the temperature difference between cases CF and CS. Immediately, we can see that there are significant changes in the distribution of temperature in the upper thermosphere of case CF. There are four ‘finger-like’ regions with local temperature increases ≥ 50 K (maximum of 175 K) and three regions with temperature decreases ≤ 40 K. These alternating temperature deviations increase with altitude and are collocated with accelerated meridional flow regions. Considering Figs. 4c and f, we see that the heating and cooling terms are now quite complex, with advective and adiabatic terms dominating ($\geq 10 \times$ Joule heating and ion drag terms). The CF thermosphere appears to be transporting heat (in ‘waves’), both equatorward and poleward from the region III/II boundary (see Fig. 3f). Achilleos et al. (1998) also shows a similar phenomenon (see top left of Fig. 9 in Achilleos et al. (1998)), whereby ‘wave-like’ patterns of high temperature are being transported away from the auroral region. The energy deposited in the auroral regions heats the local thermosphere which increases local pressure gradients. Advection then attempts to redistribute this heat which momentarily cools

the local area until enough heat is deposited again and the process restarts.

Figs. 4g-i show powers per unit area as functions of ionospheric latitude, calculated using Eqs. (4 - 8), for cases CS, CH and CF, respectively. Integrating these powers over the hemisphere gives the global powers shown in Fig. 5. Powers are indicated by legends on figures. In case CS, magnetospheric power (power used to accelerate magnetospheric plasma) is dominant up to $\sim 73^\circ$, where atmospheric power (sum of Joule heating and ion drag) quickly dominates for all poleward latitudes (see Fig. 4g). This indicates that relatively expanded M-I systems (in steady-state) generally dissipate more heat in the atmosphere than in acceleration of outward-moving plasma (Yates et al., 2012a). For case CH, Fig. 4h, we see the effects of plasma super-corotation in region III, where magnetospheric power reverses (now negative), heat dissipated as Joule heating doubles (as shown above), positive ion drag decreases by $\sim 70\%$ and negative ion drag increases by two orders of magnitude. Powers decrease in region II due to the decrease in flow shear (see Fig. 1a). In case CF, powers per unit area closely resemble those for case CS. There are small increases in peak magnetospheric power ($\sim 10\%$) and Joule heating ($\sim 25\%$) leading to an overall maximum increase in available power of $\sim 10\%$. These findings are represented on a global scale in Fig. 5.

Overall, midway through a transient compression, magnetospheric plasma super-corotates, which leads to energy being transferred from the magnetosphere to the thermosphere. Our results indicate that ~ 2000 TW of total power (magnetospheric and atmospheric) is gained by the coupled system as a result of plasma super-corotation. Note that this is considerably larger than the ~ 325 TW (closed and open field regions) calculated in Cowley et al. (2007) for a responsive thermosphere scenario. This energy transfer from the magnetosphere would act to, essentially ‘spin up’ the planet (Cowley et al., 2007) and increase the thermospheric temperature. In case CF, plasma is not super-corotating; thus the picture is fairly similar to case CS. The main difference is that there is a $\sim 20\%$ increase in total power dissipated in the atmosphere and in acceleration of the magnetosphere. This arises from increases in flow shear due to the ‘lagging’ thermosphere (see Fig. 1) and inevitably leads to the local temperature increases seen in Fig. 3i and discussed above. The finite time required for thermospheric response results in the described ‘residual’ perturbations to the initial system (CS) even after the pulse has

subsided (CF).

4. Magnetospheric Expansions

In this section we present auroral and thermospheric heating results for a transient expansion event. We present results from three periods throughout the transient event: i) Steady state (case ES with $R_{MM}=45 R_J$), ii) ‘half-pulse’ (case EH with $R_{MM}= 85 R_J$) and, iii) ‘full-pulse’ (case EF with $R_{MM}=45 R_J$).

4.1. Auroral response

We begin by investigating how a transient magnetospheric expansion affects the aurorae. Thus, we only discuss the effects on FAC densities and the precipitating energy flux. For the detailed response of M-I coupling currents, the reader is referred to Paper 1.

As for the case of our compression scenario, we summarise here the response of FAC densities (see Paper 1 for detailed discussion). Fig. 6a shows the variation of FAC density with ionospheric latitude for cases ES (solid line), EH (dashed line) and EF (dot-dashed line). Magnetospheric regions (region III shaded) are separated by black dotted lines and the latitudinal size of a HST ACS-SBC pixel is indicated by the dark grey rectangle. Case EF exhibits only minor differences with case ES, which result from the lag in the thermospheric response to transient magnetospheric changes. For case EH, the magnetospheric expansion causes the magnetic field strength (in the magnetodisc) and plasma angular velocity to decrease. Flow shear ($\Omega_T - \Omega_M$) thus increases and results in a broad region of upward FAC from $\sim 69^\circ$ to $\sim 74^\circ$ latitude. We also note a $\sim 15\%$ increase in peak FAC density in this broad upward region. At the region III/II boundary there is a small region of strong downward FAC produced by large gradients in Ω_M and Σ_P across this boundary. We also note that poleward of region III, only downward FACs exist due to the small imposed change in Ω_M in regions II and I.

We interpret our FAC density profiles by considering the corresponding precipitating electron energy fluxes, shown in Fig. 6b. Fluxes are plotted as functions of latitude. The line style code and labels are the same as in Fig. 6a and the grey solid line indicates the limit of present HST detectability (~ 1 kR; Cowley et al. (2007)). We begin by comparing cases ES and EF,

which are almost identical except between $\sim 71^\circ$ and $\sim 73^\circ$ latitude. These differences are caused by the finite thermospheric response time. Both profiles peak at $\sim 74^\circ$ latitude, equivalent to the location of the ‘main auroral oval’, and at $\sim 80^\circ$, the boundary between open (region I) and closed field lines (region II). Therefore, we would expect a fairly bright auroral oval of ~ 88 kR for case ES and ~ 79 kR for case EF. The electron energy flux for case EF is $\sim 10\%$ smaller than case ES due to $\Omega_T(ES) > \Omega_T(EF)$ leading to a smaller flow shear. Our model also predicts the possibility of observable polar emission (region II/I boundary) of ~ 15 kR for both cases ES and EF. However, this region is strongly dependent on the model used and poorly constrained by observations.

We now discuss the response of the energy flux E_f midway through our transient expansion event. The case EH profile, poleward of $\sim 74^\circ$ latitude, lies entirely below the limit of detectability due to the downward (negative) FAC density in this region. In region III, there are now two peaks, separated by $\sim 1^\circ$. The first peak, located at $\sim 73^\circ$ is $\sim 37\%$ larger than the second one, at $\sim 74^\circ$. These peaks result from the large degree of magnetospheric sub-corotation in region III (evident in Fig. 1b). Comparing case EH with the equivalent expansion case in Cowley et al. (2007), case EH, in region III, has a maximum value of E_f that is twice that in Cowley et al. (2007). This study represents the thermosphere with a GCM which responds independently to Ω_M profiles. Our results indicate that this response is not as strong as that in Cowley et al. (2007), who use a simple ‘slippage’ relation to model the thermospheric angular velocity. At the open-closed field line (region II/I) boundary, Cowley et al. (2007) obtain large energy fluxes due to their large change in Ω_M across these regions; in our study, we obtain negligible changes in E_f due to our smaller change in imposed Ω_M across this boundary.

Considering the auroral response in case EH, we expect to see no polar emission (a darkening from case ES) at the region II/I boundary. In region III, we expect a $\sim 1^\circ$ equatorward shift along with a small increase (~ 40 kR) in peak main oval brightness compared to case ES. We also note the possible observation of a somewhat bifurcated main oval; with emission peaking at $\sim 73^\circ$ and $\sim 74^\circ$ latitude. The main oval would also be considerably broader ($\sim 2\text{--}3^\circ$) as a result of the large increase in the spatial region of magnetospheric sub-corotation. Clarke et al. (2009) observed little change in auroral

brightness near the arrival of a solar wind rarefaction region, however Nichols et al. (2009) have seen changes in main oval location. The total UV power in case EH is ~ 270 GW (compared to ~ 78 GW in case ES). While this power is considerably smaller than that in case CH, it is comparable to UV powers calculated in Clarke et al. (2009) and Nichols et al. (2009), following solar wind rarefactions ($\sim 200 - 400$ GW)..

4.2. Thermospheric heating

In this section, we present and discuss the response of thermospheric heating terms to our transient expansion event. We present azimuthal and meridional flows and temperature differences in Fig. 7. The results in Fig. 7 have been discussed at length in Paper 1, and we therefore only describe the major flow patterns associated with zonal (Figs. 7a-c) and meridional directions (Figs. 7d-f). Thermospheric heating terms and powers per unit area are presented in Fig. 8 and we use Figs. 7g-i to aid in their discussion. For completeness, we also present integrated powers per hemisphere in Fig. 9. Cases ES, EH and EF are represented in respective columns 1–3 of Figs. 7-8.

Figs. 7a-c show the variation of thermospheric azimuthal velocity, in the corotating reference frame, with altitude and latitude for cases ES, EH and EF. Positive velocities represent super-corotation whilst negative velocities indicate sub-corotation. The white contour indicates the locus of rigid corotation and the black arrows indicate the direction of meridional flow. Magnetospheric regions are labelled and separated by black dotted lines. The zonal flow patterns are as in section 3.2 i.e a low altitude super-corotating jet in region III and a large sub-corotating jet spanning regions III-I. We note that the area experiencing strong super-corotation (black contour) is at a minimum in case EH and that the degree of sub-corotation decreases as the system responds to the event. Figs. 7d-f show thermospheric meridional velocity as a function of altitude and latitude for cases ES-EF. Labels, arrows and contours are the same as in Figs. 7a-c. The steady-state flow pattern, consisting of high-altitude equatorward flows and low-altitude poleward flows, is as in case CS (discussed in Smith et al. (2007); Smith and Aylward (2009); Yates et al. (2012a) and Paper 1). As the system progresses through the expansion event, the high altitude meridional flow reverses for parts of regions III and II and all of I. Large, localised acceleration regions also develop. For further details on thermospheric flows, the reader is referred to

Fig. 7g shows temperature as a function of altitude and latitude for case ES. Figs. 7h-i show the difference in thermospheric temperature between cases EH and ES, and cases EF and ES, as functions of altitude and latitude. Magnetospheric regions are labelled and separated by black dotted lines and temperatures are indicated by the colour bar. We interpret the response of thermospheric temperature with the aid of Figs. 8a-f, showing contour plots for various thermospheric heating (Figs. 8a-c) and cooling (Figs. 8d-f) terms (see plot legends for details).

Fig. 7g shows similar results to those described in section 3.2. The main difference is related to the polar ‘hotspot’ which is considerably cooler (peak temperature of ~ 590 K) than that for case CS (peak temperature ~ 705 K). As previously discussed, the ‘hotspot’ results from the meridional transport, via poleward accelerated flows, of Joule heating from lower latitudes (~ 73 – 84° ; see Figs. 8a and d) (Smith and Aylward, 2009; Yates et al., 2012a).

Fig. 7h exhibits the temperature difference between cases EH and ES. The figure shows a ~ 50 K local temperature increase at low altitudes (< 700 km) in regions III and II. This is caused by a $\geq 4\times$ increase in Joule heating and ion drag power in this region (see Figs. 7b and e). Also evident are two more minor temperature variations: i) ~ 10 K decrease at high altitude, centred on the region III/II boundary and, ii) ~ 10 K increase in the polar ‘hotspot’ region. We interpret that this local ‘cold spot’ arises mainly from the appearance of meridional accelerated flows, which efficiently transport heat away (equatorward and poleward) from the region III/II boundary, and the factor of three increase in adiabatic cooling. We attribute the small increase in temperature at the polar ‘hotspot’ to the 35 % increase in low altitude meridional velocity (itself due to poleward acceleration - more detail in Paper 1).

Fig. 7i shows the temperature difference between cases EF and ES. The temperature profile has changed significantly from that in Fig. 7h. There are two regions where temperatures increase by up to ~ 50 K: i) extending from ~ 73 – 85° latitude and low altitudes in regions III and II, and all altitudes in region I (these map to the large poleward-accelerated region in Fig. 7f); and ii) high-altitude (> 600 km) region, centred at $\sim 66^\circ$ latitude. These regions

are primarily heated by horizontal advection (high-altitude only) and adiabatic terms (all altitudes) as shown in Fig. 8c; these terms have increased from case ES by, at most, 800 % and 500 % respectively. The final feature of note in Fig. 7i is the region cooled by up to ~ -22 K, lying between the two heated regions at altitudes >550 km. This cooling is caused by a combination of local increases in horizontal advection and adiabatic cooling, by factors of three and greater. Similar to case CF, case EF's meridional flows seem to be transporting heat equatorward and poleward, although the majority of these flows act to transport thermal energy poleward.

Figs. 8g-i show powers per unit area as functions of ionospheric latitude for cases ES-EF respectively. Integrating these powers over the hemisphere gives the global powers in Fig. 9. Power sources are indicated by the legends on the figures. Fig. 8g shows the energy balance in the thermosphere for case ES. As discussed in Yates et al. (2012a), most of the energy in region III is expended in accelerating magnetospheric plasma; in region II we have a situation where magnetospheric power and atmospheric power (the sum of Joule heating and ion drag) are equal, due to $\Omega_M = 0.5 \Omega_J$. Atmospheric power is dominant in region I. For case EH (Fig. 8h), the magnetospheric power is dominant up to $\sim 73^\circ$ latitude; atmospheric power, primarily Joule heating, then dominates at all poleward latitudes. This results from the large increase in flow shear ($\Omega_T - \Omega_M$). The magnetosphere of case EF super-corotates, compared to the thermosphere, at latitudes $\leq 73^\circ$. This causes a reversal in energy transfer, which now flows from magnetosphere to atmosphere (see Fig. 8i). Polewards of 73° , the energy balance is similar to that of case ES.

We conclude that a transient magnetospheric expansion creates a significant increase in both power dissipated in the atmosphere due to Joule heating ($\sim 6\times$ that of ES) and ion drag ($\sim 3\times$ that of ES). Moreover, the power used to accelerate the magnetosphere towards corotation is $\sim 7\times$ that of ES, and is shown in Fig. 9. These increases lead to a total power per hemisphere of ~ 2600 TW which is three times larger than the responsive thermosphere case in Cowley et al. (2007). These changes in heating and cooling create the local temperature increases discussed above, but only by $\lesssim 7$ K (compared to case ES). For case EF, where we now have the magnetosphere rotating faster than the thermosphere, there is a $\sim 75\%$ decrease in the magnitude of ‘magnetospheric’ power. The magnetosphere is thus transferring power to the thermosphere in this case, albeit a relatively small amount. This effec-

tively ‘pulls’ the thermosphere along, increasing its angular velocity in order to return to the steady-state situation where $\Omega_T > \Omega_M$. We note that energy dissipated via Joule heating also decreases slightly due to the small decrease in flow shear. Overall, then, the total power per hemisphere in case EF is only 30 % that of case ES.

5. Conclusion

This study models the effects of transient changes in solar wind dynamic pressure on Jovian auroral parameters and the thermospheric energy budget. A companion study, considering the response of M-I coupling currents and thermospheric dynamics is presented in Paper 1. The transient changes simulated are two types: i) a transient compression event, and ii) a transient expansion event. Both events are assumed to last for three hours, and we have presented and compared pre-event, midway (maximum compression or expansion) and post-event results in sections 3 and 4.

Simulations of the auroral response to a transient compression and the subsequent return to the initial magnetospheric configuration showed significant variation in auroral size, location and brightness. Midway through the compression event we find that auroral brightness, estimated from the precipitating electron energy flux, increases from ~ 600 kR (in steady state) to ~ 2800 kR. The location of the main auroral oval also shifts poleward by $\sim 0.2^\circ$ latitude and its width shrinks slightly compared to the steady-state. Observations by Clarke et al. (2009) and Nichols et al. (2009) find factor-of-two increases in auroral brightness as well as poleward shifts of up to $\sim 1^\circ$ (Nichols et al., 2009) due to the arrival of solar wind shocks. The total UV power can also be used to examine the auroral response, and we find that UV powers are approximately a factor of two or three larger than those observed by Clarke et al. (2009) and Nichols et al. (2009). This is interesting as their observed compressions (magnetopause change of $\sim 40 R_J$) are larger than our modelled one (magnetopause change of $\sim 33 R_J$). Immediately after the transient compression event, we find that the aurora differs slightly from the initial steady-state, and then only in regions mapping to the middle magnetosphere. There is an increase in auroral emission of ~ 200 kR ($\sim 35\%$) and a $\sim 1.5^\circ$ broadening of the main oval.

The super-corotation of magnetospheric plasma midway through the compression event caused various changes in thermospheric heating and cooling terms. Joule heating increases by a factor of two and negative ion drag (decreases kinetic energy of the system) increases by a factor of seven, whilst positive ion drag (increase kinetic energy of the system) is halved. Overall, the magnetospheric super-corotation results in ~ 2000 TW resultant power being dissipated in the thermosphere. This leads to local temperature changes of ~ 25 K. After the transient event subsides, adiabatic and horizontal advective terms dominate over Joule heating and ion drag by an order of magnitude. This results in high-altitude thermospheric temperature increases of ≥ 40 K.

Our transient expansion simulations show less auroral variation than the compression simulations. At maximum expansion, peak auroral brightness increases from ~ 88 kR to ~ 126 kR and shifts equatorwards by $\sim 1^\circ$ latitude. We do note, however, the presence of a slightly smaller auroral peak, approximately 1° poleward, creating a slight bifurcation of the main oval. The latitudinal width of the main oval also increased by $\sim 2-3^\circ$. We would thus expect to observe a broad, slightly ‘bifurcated’ main oval and no significant polar emission midway through the expansion event. Observations of the auroral response near solar wind rarefaction regions by Clarke et al. (2009) have shown that there is little, if any, corresponding change in auroral brightness. As the expansion event subsides, we see only a small difference between the initial auroral profile and the final one. This difference is a small 10 % decrease in peak auroral emission, caused by the ‘lagging’ thermospheric response.

The transient magnetospheric expansion, similar to the compression, increased the total energy available to the thermosphere-magnetosphere system. The expansion lead to a factor-of-four increase in ion drag power and Joule heating rate (in the region mapped to the middle magnetosphere), which resulted in local temperature increases $\lesssim 50$ K. Globally, the large degree of magnetospheric sub-corotation increased the power expended in accelerating the magnetospheric plasma by a factor of seven. This aspect coupled with the changes in Joule heating, produced a ~ 2170 TW increase in the total power dissipated and used by the thermosphere. At the end of the expansion event, horizontal advection and adiabatic heating terms dominate, and are on average 650 % larger than in steady-state. This creates large areas of temperature variation $\lesssim 50$ K. Globally, due to the magnetosphere

rotating slightly faster than the thermosphere, the total power dissipated in the coupled system decreases significantly to ~ 125 TW ($\sim 30\%$ of the total in steady-state).

In summary, by examining our model’s meridional flows and temperature distributions, we find that, by the end of the imposed transient changes, heat (thermal energy) has started to be transported both poleward and equatorward, particularly at high altitudes, in accordance with studies by Waite et al. (1983) and Melin et al. (2006). At present, though promising, these results are unable to explain the high thermospheric temperatures observed at low latitudes in Jupiter (~ 900 K; Seiff et al. (1998)). As part of future studies, it would be interesting to vary the duration of these transient events and to experiment with a more realistic solar wind profile, in order to model the dynamic response of the Jovian thermosphere over more extended periods of time.

Acknowledgement

JNY was supported by an STFC studentship award. The authors acknowledge support of the STFC funded Miracle Consortium (part of the DiRAC facility) in providing access to computational resources. The authors express their gratitude to Chris Smith who developed the GCM used herein. JNY would also like to thank J. D. Nichols for useful discussions.

References

- Achilleos, N., Miller, S., Tennyson, J., Aylward, A. D., Mueller-Wodarg, I., Rees, D., 1998. JIM: A time-dependent, three-dimensional model of Jupiter’s thermosphere and ionosphere. *J. Geophys. Res.* 103, 20089–20112.
- Clarke, J. T., Nichols, J., Gérard, J.-C., Grodent, D., Hansen, K. C., Kurth, W., Gladstone, G. R., Duval, J., Wannawichian, S., Bunce, E., Cowley, S. W. H., Crary, F., Dougherty, M., Lamy, L., Mitchell, D., Pryor, W., Retherford, K., Stallard, T., Zieger, B., Zarka, P., Cecconi, B., May 2009. Response of Jupiter’s and Saturn’s auroral activity to the solar wind. *Journal of Geophysical Research (Space Physics)* 114, 5210.
- Cowley, S. W. H., Alexeev, I. I., Belenkaya, E. S., Bunce, E. J., Cottis, C. E., Kalegaev, V. V., Nichols, J. D., Prangé, R., Wilson, F. J., 2005. A

- simple axisymmetric model of magnetosphere-ionosphere coupling currents in Jupiter's polar ionosphere. *J. Geophys. Res.* 110, 11209–11226.
- Cowley, S. W. H., Bunce, E. J., 2003a. Modulation of Jovian middle magnetosphere currents and auroral precipitation by solar wind-induced compressions and expansions of the magnetosphere: initial response and steady state. *Planet. Space Sci.* 51, 31–56.
- Cowley, S. W. H., Bunce, E. J., 2003b. Modulation of Jupiter's main auroral oval emissions by solar wind induced expansions and compressions of the magnetosphere. *Planet. Space Sci.* 51, 57–79.
- Cowley, S. W. H., Nichols, J. D., Andrews, D. J., 2007. Modulation of Jupiter's plasma flow, polar currents, and auroral precipitation by solar wind-induced compressions and expansions of the magnetosphere: a simple theoretical model. *Ann. Geophys.* 25, 1433–1463.
- Eviatar, A., Barbosa, D. D., Sep. 1984. Jovian magnetospheric neutral wind and auroral precipitation flux. *J. Geophys. Res.* 89, 7393–7398.
- Gong, B., 2005. Variations of Jovian aurora induced by changes in solar wind dynamic pressure. Ph.D. thesis, Rice University.
- Grodent, D., Gérard, J., 2001. A self-consistent model of the Jovian auroral thermal structure. *J. Geophys. Res.* 106, 12933–12952.
- Hill, T. W., 1979. Inertial limit on corotation. *J. Geophys. Res.* 84, 6554–6558.
- Hill, T. W., 2001. The Jovian auroral oval. *J. Geophys. Res.* 106, 8101–8108.
- Knight, S., May 1973. Parallel electric fields. *Planet. Space Sci.* 21, 741–750.
- Lundin, R., Sandahl, I., Jun. 1978. Some characteristics of the parallel electric field acceleration of electrons over discrete auroral arcs as observed from two rocket flights. In: Halvorsen, T., Battrick, B. (Eds.), *European Sounding Rocket, Balloon and Related Research, with Emphasis on Experiments at High Latitudes*. Vol. 135 of ESA Special Publication. pp. 125–136.

- Melin, H., Miller, S., Stallard, T., Smith, C., Grodent, D., Mar. 2006. Estimated energy balance in the jovian upper atmosphere during an auroral heating event. *Icarus* 181, 256–265.
- Miller, S., Achilleos, N., Ballester, G. E., Geballe, T. R., Joseph, R. D., Prangé, R., Rego, D., Stallard, T., Tennyson, J., Trafton, L. M., Waite, Jr., J. H., 2000. The role of H^+_3 in planetary atmospheres. In: *Astronomy, physics and chemistry of H^+_3* . Vol. 358 of Royal Society of London Philosophical Transactions Series A. p. 2485.
- Millward, G., Miller, S., Stallard, T., Achilleos, N., Aylward, A. D., Jan. 2005. On the dynamics of the jovian ionosphere and thermosphere. *Icarus* 173, 200–211.
- Moore, L. E., Mendillo, M., Müller-Wodarg, I. C. F., Murr, D. L., Dec. 2004. Modeling of global variations and ring shadowing in Saturn’s ionosphere. *Icarus* 172, 503–520.
- Müller-Wodarg, I. C. F., Mendillo, M., Yelle, R. V., Aylward, A. D., Jan. 2006. A global circulation model of Saturn’s thermosphere. *Planet. Space Sci.* 180, 147–160.
- Nichols, J., Cowley, S., 2004. Magnetosphere-ionosphere coupling currents in Jupiter’s middle magnetosphere: effect of precipitation-induced enhancement of the ionospheric Pedersen conductivity. *Ann. Geophys.* 22, 1799–1827.
- Nichols, J. D., Clarke, J. T., Gérard, J. C., Grodent, D., Hansen, K. C., Jun. 2009. Variation of different components of Jupiter’s auroral emission. *Journal of Geophysical Research (Space Physics)* 114, 6210.
- Phillips, J. L., Bame, S. J., Barraclough, B. L., McComas, D. J., Forsyth, R. J., Canu, P., Kellogg, P. J., Nov. 1993a. Ulysses plasma electron observations in the Jovian magnetosphere. *Planet. Space Sci.* 41, 877–892.
- Phillips, J. L., Bame, S. J., Thomsen, M. F., Goldstein, B. E., Smith, E. J., Dec. 1993b. ULYSSES plasma observations in the Jovian magnetosheath. *J. Geophys. Res.* 98, 21189.
- Pontius, D. H., 1997. Radial mass transport and rotational dynamics. *J. Geophys. Res.* 102, 7137–7150.

- Scudder, J. D., Sittler, E. C., Bridge, H. S., Sep. 1981. A survey of the plasma electron environment of Jupiter - A view from Voyager. *J. Geophys. Res.* 86, 8157–8179.
- Seiff, A., Kirk, D. B., Knight, T. C. D., Young, R. E., Mihalov, J. D., Young, L. A., Milos, F. S., Schubert, G., Blanchard, R. C., Atkinson, D., 1998. Thermal structure of Jupiter’s atmosphere near the edge of a 5- μ m hot spot in the north equatorial belt. *J. Geophys. Res.* 103, 22857–22890.
- Smith, C. G. A., 2006. Modelling the Thermosphere of the Giant Planets. Ph.D. thesis, University College London.
- Smith, C. G. A., Aylward, A. D., 2008. Coupled rotational dynamics of Saturn’s thermosphere and magnetosphere: a thermospheric modelling study. *Ann. Geophys.* 26, 1007–1027.
- Smith, C. G. A., Aylward, A. D., 2009. Coupled rotational dynamics of Jupiter’s thermosphere and magnetosphere. *Ann. Geophys.* 27, 199–230.
- Smith, C. G. A., Aylward, A. D., Millward, G. H., Miller, S., Moore, L. E., 2007. An unexpected cooling effect in Saturn’s upper atmosphere. *Nature* 445, 399–401.
- Smith, C. G. A., Miller, S., Aylward, A. D., 2005. Magnetospheric energy inputs into the upper atmospheres of the giant planets. *Ann. Geophys.* 23, 1943–1947.
- Stallard, T., Miller, S., Millward, G., Joseph, R. D., Dec. 2001. On the Dynamics of the Jovian Ionosphere and Thermosphere. I. The Measurement of Ion Winds. *Icarus* 154, 475–491.
- Stallard, T., Miller, S., Millward, G., Joseph, R. D., Apr. 2002. On the Dynamics of the Jovian Ionosphere and Thermosphere. II. The Measurement of H_3^+ Vibrational Temperature, Column Density, and Total Emission. *Icarus* 156, 498–514.
- Stallard, T. S., Miller, S., Cowley, S. W. H., Bunce, E. J., Mar. 2003. Jupiter’s polar ionospheric flows: Measured intensity and velocity variations poleward of the main auroral oval. *Geophys. Res. Lett.* 30 (5), 050000–1.

- Strobel, D. F., Smith, G. R., 1973. On the temperature of the Jovian thermosphere. *Journal of Atmospheric Sciences* 30, 718–725.
- Tao, C., Fujiwara, H., Kasaba, Y., 2009. Neutral wind control of the Jovian magnetosphere-ionosphere current system. *J. Geophys. Res.* 114, 8307–8323.
- Waite, J. H., Cravens, T. E., Kozyra, J., Nagy, A. F., Atreya, S. K., Chen, R. H., Aug. 1983. Electron precipitation and related aeronomy of the Jovian thermosphere and ionosphere. *J. Geophys. Res.* 88, 6143–6163.
- Yates, J., Achilleos, N., Guio, P., 2012a. Influence of upstream solar wind on thermospheric flows at jupiter. *Planetary and Space Science* 61 (1), 15 – 31, surfaces, atmospheres and magnetospheres of the outer planets and their satellites and ring systems: Part VII.
- Yates, J., Achilleos, N., Guio, P., 2012b. Response of the jovian thermosphere to a transient ‘pulse’ in solar wind pressure. *Planetary and Space Science*, submitted.
- Yelle, R. V., Miller, S., 2004. Jupiter’s thermosphere and ionosphere. pp. 185–218.
- Young, L. A., Yelle, R. V., Young, R., Seiff, A., Kirk, D. B., Apr. 1997. Gravity waves in Jupiter’s thermosphere. *Science* 276, 108–111.

Table 1: Magnetospheric electron source parameters. This table is adapted from Table 1, Cowley et al. (2007). N_e represents the electron density, W_{th} the electron thermal energy, $j_{||i0}$ the unaccelerated current density and E_{f0} the unaccelerated energy flux.

Parameter	Open field lines	Outer magnetosphere	Middle magnetosphere
N_e / cm^{-3}	0.5	0.02	0.01
W_{th} / keV	0.05	0.25	2.5
$j_{ i0} / \mu\text{A m}^{-2}$	0.095	0.0085	0.013
$E_{f0} / \text{mW m}^{-2}$	0.0095	0.0042	0.067

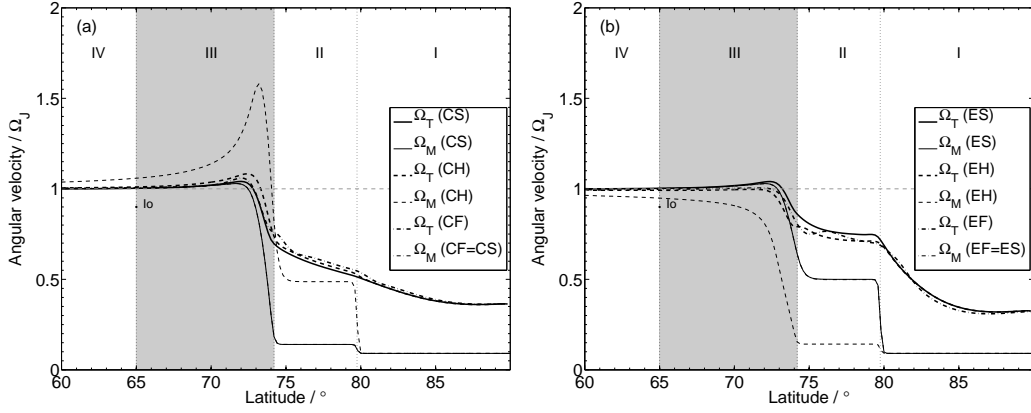


Figure 1: (a) Thermospheric and plasma angular velocity profiles for the transient compression cases as a function of ionospheric latitude. Thick lines represent thermospheric profiles whilst thin lines represent plasma profiles. The solid lines represent case CS (steady state before compression) whilst the dashed and dot-dashed lines indicate cases CH (system at minimum disc radius) and CF (system just returned to initial disc radius) respectively. The magnetospheric regions (region III shaded) are labelled and separated by the black dotted lines. The magnetically mapped location of Io on the ionosphere is marked and labelled. (b) Thermosphere and plasma angular velocity profiles for the transient expansion cases as a function of ionospheric latitude. The line styles are the same as (a) but the cases are now ES, EH and EF respectively, where ‘E’ denotes expansion, and the ‘S’, ‘H’ and ‘F’ symbols represent the same phases of the event as for Fig. 1a. This Figure is the same as Fig.2 in Paper 1.

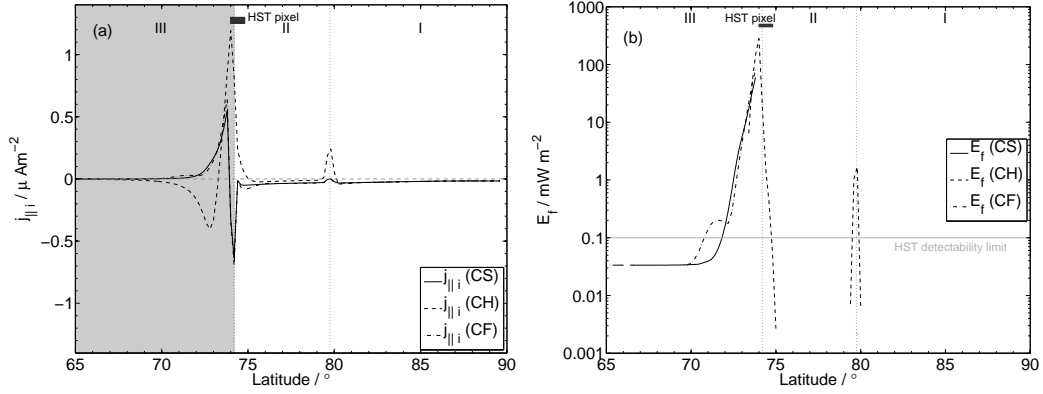


Figure 2: (a) FAC densities in the high latitude ionospheric region for our transient compression cases. The solid line represents case CS whilst the dashed and dot-dashed lines indicate cases CH and CF respectively. The conjugate magnetospheric regions (region III is shaded) are separated by dotted black lines and labelled. The latitudinal size of an ACS-SBC HST pixel located near the main auroral emission is represented by the dark grey box. This Figure is the same as Fig.4 in Paper 1. (b) Shows the latitudinal variation of the precipitating electron flux for the transient compression cases. The colour codes and in plot labels are the same as (a). The solid grey line indicates the limit of detectability of the HST (Cowley et al., 2007).

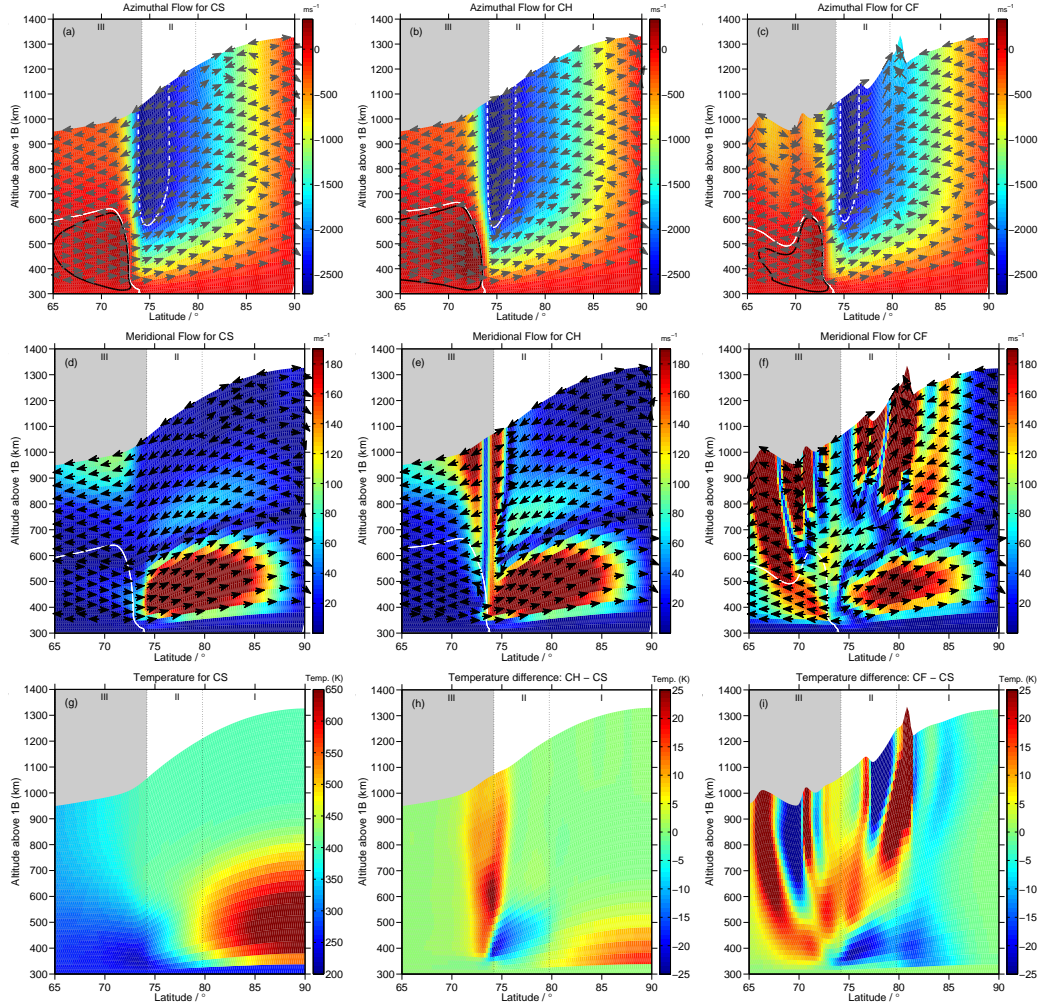


Figure 3: (a)-(c) show the variation of thermospheric azimuthal velocity (colour scale) in the corotating reference frame for cases CS, CH and CF respectively (left to right). Positive values (dark red) indicate super-corotation, whilst negative values (light red to blue) indicate sub-corotation. The arrows show the direction of meridional flow and the white line indicates the locus of rigid corotation. The solid black encloses regions of super-corotation ($> 25 \text{ m s}^{-1}$) and the dashed white line encloses regions that are sub-corotating at a rate $> -2500 \text{ m s}^{-1}$. The magnetospheric regions (region III shaded) are separated by dotted black lines and labelled. (d)-(f) show the meridional velocity in the thermosphere for cases CS-CF. The colour scale indicates the speed of flows. All other labels and symbols are as for (a)-(c). (g) shows the thermospheric temperature distributions for case CS whilst (h)-(i) show the temperature difference between cases CH and CS; and between cases CF and CS. Other labels are as in (a)-(c). This Figure is the same as Fig.6 in Paper 1.

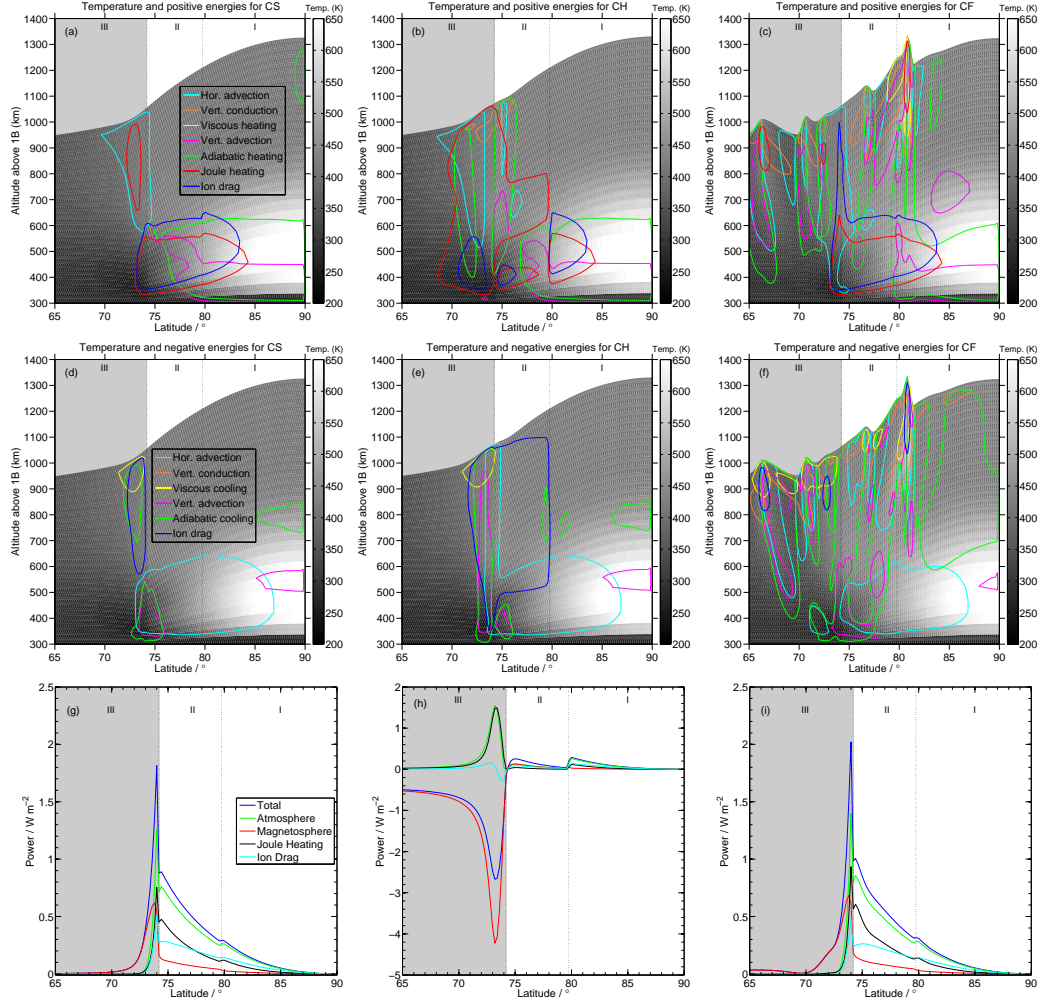


Figure 4: (a)-(c) shows the variation of atmospheric heating terms with altitude, latitude and temperature (colour bar) for cases CS, CH and CF (left to right). The contours enclose regions where heating/kinetic energy rates exceed 20 W kg^{-1} . Ion drag, Joule heating, vertical and horizontal advection of energy, adiabatic heating/cooling, viscous heating and heat conduction (vertical and turbulent) are represented by blue, red, yellow and magenta, green, cyan and orange lines. The magnetospheric regions are separated and labelled. (d)-(f) show the variation of atmospheric cooling terms where the contours enclose regions where heating/kinetic energy are decreasing (cooling) with rates exceeding 20 W kg^{-1} . All colours and labels are as in (a)-(c). (g)-(i) show how the power per unit area varies for our transient compression cases. The blue line represents total power which is the sum of magnetospheric power (red line) and atmospheric power (green line); atmospheric power is the sum of both Joule heating (black solid line) and ion drag (cyan solid line). Other labels are as for (a)-(c).

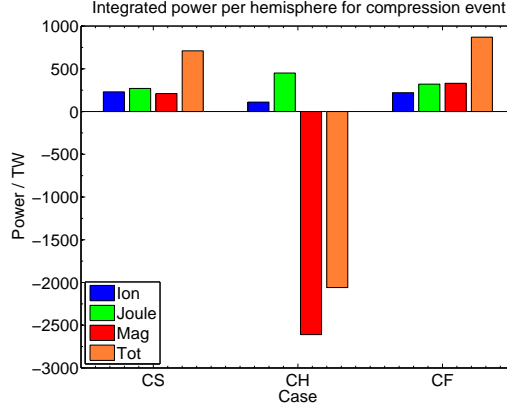


Figure 5: Integrated ionospheric powers per hemisphere for cases CS-CF are represented in this figure. Ion drag is represented by blue bars, Joule heating by green bars, magnetospheric power by red bars and total (sum of all above) is represented by orange bars. See text for further detail.

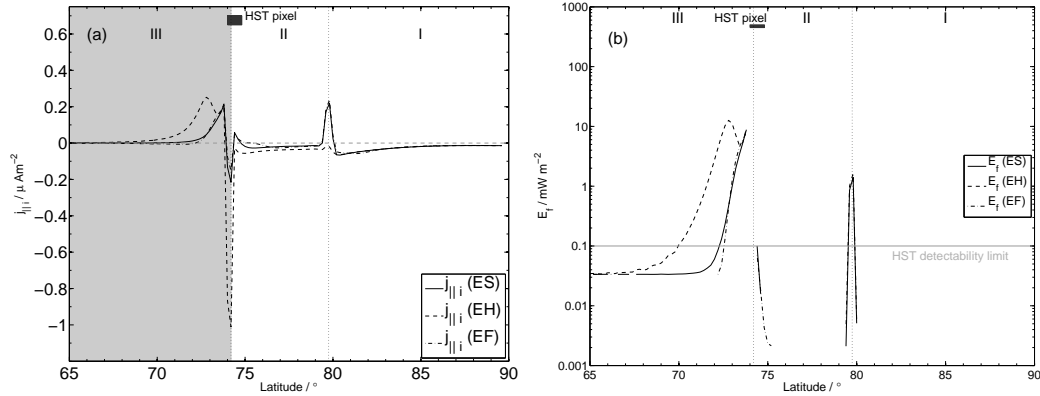


Figure 6: FAC densities in the high latitude region for our transient expansion cases. The solid line represents case ES whilst the dashed and dot-dashed lines indicate cases EH and EF respectively. The magnetospheric regions (region III is shaded) are separated by dotted black lines and labelled. The latitudinal size of an ACS-SBC HST pixel is indicated by the dark grey box. This Figure is the same as Fig.8 in Paper 1. (b) Shows the latitudinal variation of the precipitating electron flux for the transient expansion cases. The colour codes and in plot labels are the same as (a).

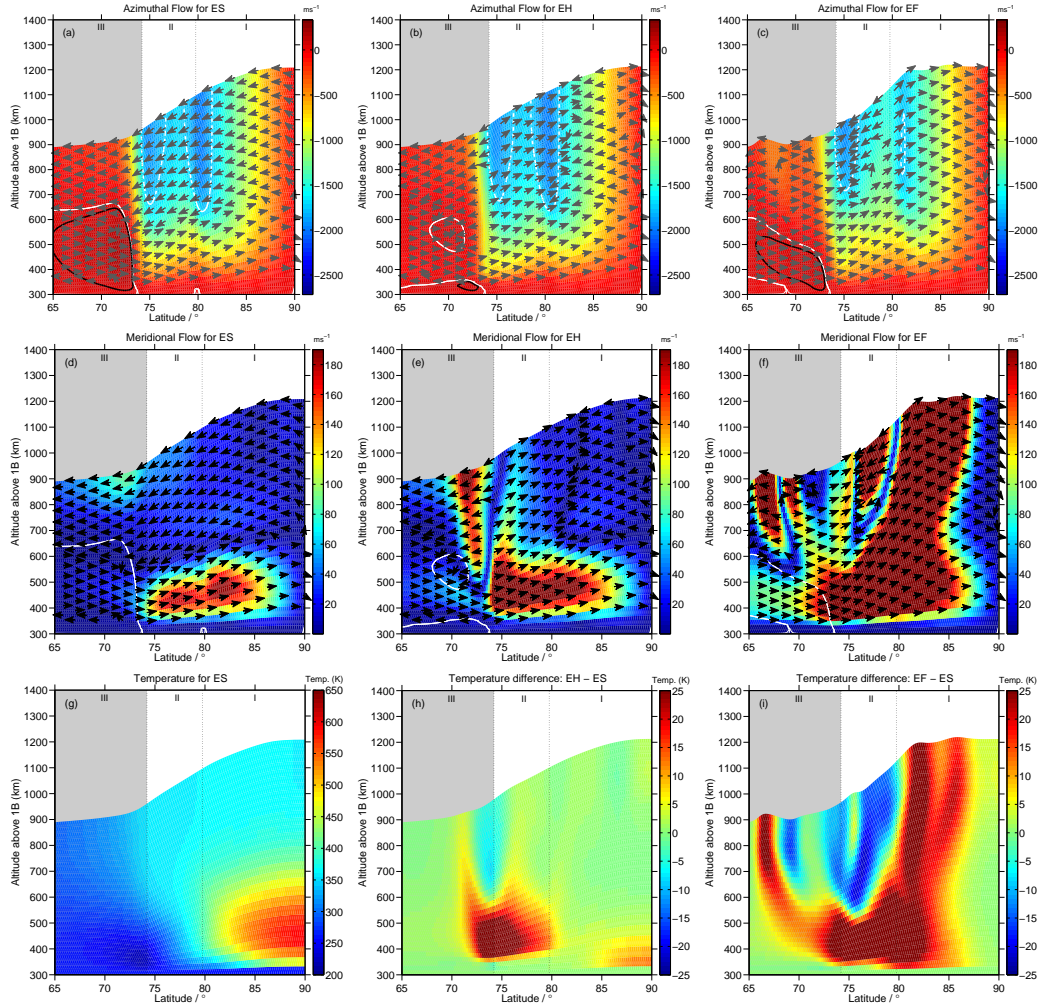


Figure 7: (a)-(c) show the variation of thermospheric azimuthal velocity (colour scale) in the corotating reference frame for cases ES-EF respectively (left to right). Positive values (dark red) indicate super-corotation, whilst negative values (light red to blue) indicate sub-corotation. The arrows show the direction of meridional flow and the white line indicates the locus of rigid corotation. The solid black encloses regions of super-corotation ($> 25 \text{ m s}^{-1}$) and the dashed white line encloses regions that are sub-corotating at a rate $> -1750 \text{ m s}^{-1}$. The magnetospheric regions (region III is shaded) are separated by dotted black lines and labelled. (d)-(f) show the meridional velocity in the thermosphere for cases ES-EF. The colour scale indicates the speed of flows. All other labels and are as for (a)-(c). (g) shows the thermospheric temperature distributions for case ES whilst (h)-(i) show the temperature difference between cases EH and EF and case ES. All labels are as in (a)-(c). This Figure is the same as Fig.9 in Paper 1.

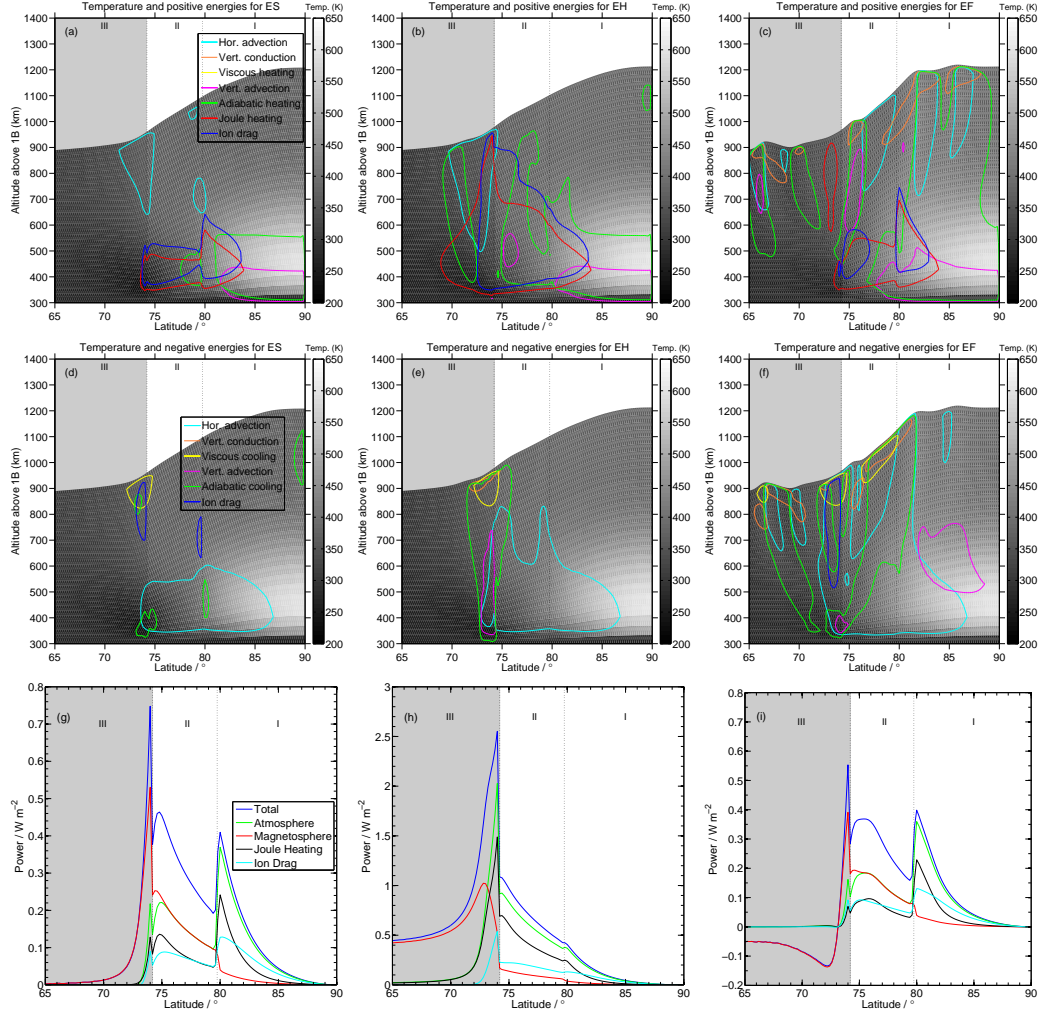


Figure 8: (a)-(c) shows the variation of atmospheric heating terms with altitude, latitude and temperature (colour bar) for cases ES, EH and EF (left to right). The contours enclose regions where heating/kinetic energy rates exceed 20 W kg^{-1} . Ion drag, Joule heating, vertical and horizontal advection of energy, adiabatic heating/cooling, viscous heating and heat conduction (vertical and turbulent) are represented by blue, red, yellow and magenta, green, cyan and orange lines. The magnetospheric regions are separated and labelled. (d)-(f) show the variation of atmospheric cooling terms where the contours enclose regions where heating/kinetic energy are decreasing (cooling) with rates exceeding 20 W kg^{-1} . All colours and labels are as in (a)-(c). (g)-(i) show how the power per unit area varies for our transient expansion cases. The blue line represents total power which is the sum of magnetospheric power (red line) and atmospheric power (green line); atmospheric power is the sum of both Joule heating (black solid line) and ion drag (cyan solid line). All other labels are as for (a)-(c).

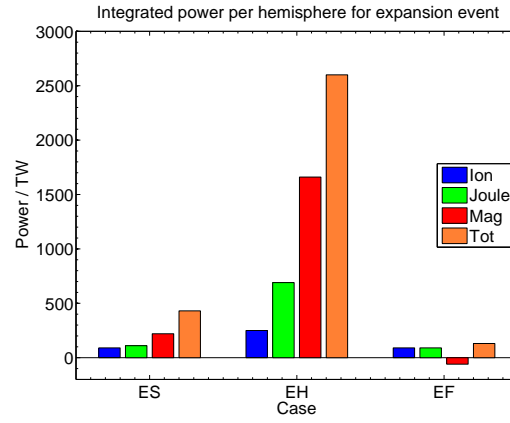


Figure 9: Integrated ionospheric powers per hemisphere for cases ES-EF are represented in this figure. Ion drag is represented by blue bars, Joule heating by green bars, magnetospheric power by red bars and total (sum of all above) is represented by orange bars.